


Article

# The Fundamental Comparison of Zn–2Mg and Mg–4Y–3RE Alloys as a Perspective Biodegradable Materials

Jiří Kubásek <sup>1</sup> , Drahomír Dvorský <sup>1</sup>, Jiří Šedý <sup>2</sup>, Šárka Msallamová <sup>1</sup>, Jitka Levorová <sup>3</sup>, René Foltán <sup>3</sup> and Dalibor Vojtěch <sup>1,\*</sup>

<sup>1</sup> Department of Metals and Corrosion Engineering, Institute of Chemical Technology, 16628 Prague, Czech Republic; Kubasekj@vscht.cz (J.K.); dvorskyd@vscht.cz (D.D.); msallams@vscht.cz (Š.M.)

<sup>2</sup> Department of Normal Anatomy, Faculty of Medicine, Palacký University Olomouc, 775 15 Olomouc, Czech Republic; jirisedy@jirisedy.cz

<sup>3</sup> Department of Oral and Maxillofacial Surgery, First Faculty of Medicine, Charles University, 128 01 Prague, Czech Republic; jitka.levorova@gmail.com (J.L.); Rene.Foltan@vfn.cz (R.F.)

\* Correspondence: vojtechd@vscht.cz

Received: 3 October 2019; Accepted: 12 November 2019; Published: 13 November 2019



**Abstract:** Biodegradable materials are of interest for temporary medical implants like stents for restoring damaged blood vessels, plates, screws, nails for fixing fractured bones. In the present paper new biodegradable Zn–2Mg alloy prepared by conventional casting and hot extrusion was tested in in vitro and in vivo conditions. Structure characterization and mechanical properties in tension and compression have been evaluated. For in vivo tests, hemispherical implants were placed into a rat cranium. Visual observation of the living animals, an inspection of implant location and computed tomography CT imaging 12 weeks after implantation were performed. Extracted implants were studied using scanning electron microscopy (SEM) on perpendicular cuts through corrosion products. The behaviour of zinc alloy both in in vitro and in vivo conditions was compared with commercially used Mg-based alloy (Mg–4Y–3RE) prepared by conventional casting and hot extrusion. Both compressive and tensile yield strengths of Zn and Mg-based alloys were similar; however, the brittleness of Mg–4Y–3RE was lower. Zn and Mg-based implants have no adverse effects on the behaviour or physical condition of rats. Moreover, gas bubbles and the inflammatory reaction of the living tissue were not detected after the 12-week period.

**Keywords:** magnesium; zinc; biodegradable materials; in-vivo tests; corrosion

## 1. Introduction

Biodegradable metals and alloys have attracted great attention in the past few decades as promising alternatives to permanent implant materials, like Ti alloys, Co alloys or stainless steels, and to biodegradable polymeric materials, such as poly-lactic acid (PLLA). Biodegradable materials are of interest for temporary medical implants like stents for restoring damaged blood vessels, plates, screws, nails for fixing fractured bones. Although the biodegradable polymeric materials can be used for coronary stent applications, the main problem is related to the load-bearing applications, where polymeric materials often fail because materials available at present suffer from a low hardness, strength, fracture toughness and wear resistance even when additions of ceramic particles are used. When using biodegradable material, instead of a permanent one, the second surgery for removing the implant is not needed after healing which reduces the morbidity, health costs, and inconvenience to

the patient. Therefore, great attention is devoted to metallic biodegradable materials, which appear more suitable for load-bearing applications.

Three metals, magnesium, iron and zinc, have been mostly studied up to date concerning the design of biodegradable medical implants because they are relatively non-toxic and essential for proper biological functions of the human body. In the case of magnesium, the research activities lasting more than one century have provided a huge amount of data related to mechanical properties, *in vitro* bio-corrosion behaviour and *in vivo* biocompatibility of these materials [1–12]. But problems with excessive *in vivo* bio-corrosion rates of Mg alloys associated with the evolution of undesirable corrosion products have precluded the widespread use of Mg in the medical field. Although commercial magnesium screws have been manufactured from Magnezix (MgYREZr alloy) [13], the actual range of use in medicine is not known. Iron also offers a potential for applications in biodegradable implants. The main advantage of Fe over Mg is a higher strength, but the ferromagnetic behaviour and insufficient *in vivo* bio-corrosion rates of Fe remain essential topics for further experimental research [14–16]. The insufficiently low corrosion rate of pure Fe can be partially increased by alloying with Mn, Pd, W, Sn, B, C, S or Si [17,18], however, in the case of Mn or Si addition, this can lead to the decrease of the viability of a specific type of cells, such as human endothelial cells (ECV304) [18–20].

There is currently only a limited number of research works dealing with *in vivo* assays of degradable stents made of iron [21–25]. These studies did not show adverse effect in tissues of rabbits and minipigs (thrombosis, necrosis, inflammation). Mueller et al. [26] studied the behaviour of iron sheets in the tails of mice. Histological examination showed slow degradation of Fe and accumulation of deposits in some places. This phenomenon has been accompanied by an inflammatory reaction but no indication of toxic effects [26].

Zinc and its alloys have been subjects of biomaterial engineering research for the last few years [15,27–30] and significant progress and huge interest in the research areas has been recorded recently [30–35]. A clear advantage of zinc and its alloys over magnesium is processing. Casting is generally performed in an air atmosphere at lower melting temperatures of about 500–600 °C. Magnesium alloys are melted at 700–800 °C in a protective atmosphere. Besides, zinc-based alloys are characterized by good machinability and can be easily processed by conventional extrusion.

Zinc exhibits similar mechanical properties like magnesium, but *in vitro* corrosion of zinc is slower in comparison with magnesium [36]. Another beneficial feature of zinc is the absence of hydrogen evolution in the corrosion process [36]. From the biological point of view, zinc is an essential element for biological functions of the human body. It is involved in various aspects of cellular metabolism, supports proper functions of numerous enzymes, immune system, protein and DNA synthesis, normal growth, wound healing, a proper sense of taste and smell [37]. The recommended dietary allowance and recommended upper limit for zinc are 15 and 40 mg per day, respectively [38], but consumption in amounts higher than these values is generally considered relatively non-toxic. Even amounts approaching 100 mg/day can be tolerated for some time [28,38].

The use of pure Zn as biodegradable material is limited due to its insufficient strength, plasticity and hardness, but this may be easily overcome by using suitable alloys.

*In vitro* biocompatibility investigation of zinc alloys including cytotoxicity tests in the alloy, extracts revealed that zinc is slightly less biocompatible to U-2 Os and L929 cells than magnesium [32,35]. Decreased viability (about 65%) of VSMC cells in alloy extract was observed by Li et al. [33], although the viability of ECV304 and MC63 cells was determined as excellent in the same study. Murni et al. [30] observed generally very good *in vitro* biocompatibility of Zn-3Mg alloy although decreased viability of NHOst primary cells at specific conditions has been observed. Also, genotoxicity and mutagenicity tests did not indicate any negative effects connected with the use of zinc [30]. *In vitro* study of pure Zn in which the authors pointed out slightly lower mechanical and cytotoxicity properties for Zn compared to the Mg was performed by Liu et al. [34]. Although the number of *in vivo* biocompatibility tests with zinc or zinc alloys is still limited [28,33,39–42], these tests indicate that zinc is a promising biodegradable material. In the study of Zberg et al. [39] an amorphous Mg–Zn–Ca alloy containing

about 50 wt % of Zn was prepared by copper-mould-injection casting. The amorphous alloy was then implanted into the abdominal cavity of domestic pigs. It was shown by histological analysis that the implants exhibited the same good tissue compatibility as pure Mg implants, but strongly reduced hydrogen evolution due to the presence of zinc. One drawback of amorphous alloys is a quite difficult preparation procedure requiring high cooling rates and, therefore, small (a few mm in thickness) amorphous samples can only be prepared. Samples of larger volumes prepared at lower cooling rates would be brittle and unsuitable for load-bearing applications, because of the presence of Mg + MgZn eutectic mixture in the structure. The *in vivo* study of pure zinc was reported by Bowen et al. [28]. They applied thin zinc wires to the abdominal aorta of adult rats and studied corrosion rates, corrosion products and tissue adherence. It was observed that the *in vivo* corrosion rate ranged between 10 and 50  $\mu\text{m}/\text{year}$  and that it progressively increased during six months' exposition. Another important finding was that the implant remained intact for four months after implantation. Corrosion products on the surface were compact facilitating a good adherence of the surrounding tissue. Bowen et al. [40] and Yang et al. [43] reported excellent biocompatibility, without severe inflammation, platelet aggregation or thrombosis formation on zinc wires or stents in the aorta of rats and rabbits, respectively.

Besides the stent applications, zinc biodegradable alloys are also being explored as potential alternatives to titanium or stainless steels for fixation devices of fractured bones in traumatology. *In vivo* study of Zn–Mg alloy in different states has been performed by Li et al. [33]. These tests confirmed the suitability of binary alloys for orthopaedic application, as it guaranteed sufficient mechanical support during the tissue-repair process.

Other novel information considering specific challenges related to zinc is summarized in several review works [44–48].

The present paper deals with the structure, mechanical properties, and *in vitro* and *in vivo* corrosion of biodegradable Zn–2Mg alloy. The magnesium addition to the experimental alloy was aimed to increase the strength and hardness, improve biocompatibility, support bone growth and slow down the corrosion rate of zinc [36,49,50]. The commercial Mg–4Y–3RE (WE43, according to the ASTM B93 designation) biodegradable alloy [51–53] was also explored as reference material. A similar alloy called Magnezix has recently been approved for clinical testing and use in human medicine [54].

## 2. Materials and Methods

The Zn–2Mg and Mg–4Y–3RE alloys were investigated in this study. Chemical compositions are given in Table 1. The Zn–2Mg alloy was prepared by melting pure metals (99.9% purity) in a resistance furnace under argon atmosphere. The temperature of the melt was kept at 500 °C to avoid excessive evaporation of zinc and oxidation of magnesium. After sufficient homogenization of the melt, it was poured to a cast-iron mould to prepare cylindrical ingots of 20 mm in diameter and 200 mm in length. The Mg–4Y–3RE alloy ingots of 40 × 80 × 500 mm<sup>3</sup> in size were purchased from an industrial supplier (Luxfer MEL Technologies, Manchester, UK). The alloy was re-melted in a vacuum induction furnace and cast to ingots of the same dimensions as those of the previous material. Before extrusion the Mg–4Y–3RE alloy was heat treated at 525 °C for 8 h. The following step was a hot extrusion of Zn–2Mg and Mg–4Y–3RE conducted at a temperature of 300 °C and 400 °C respectively, extrusion rate of 5 mm/min and extrusion ratio of 10:1 to produce rods of 6 mm in diameter and 80 mm in length.

**Table 1.** Chemical compositions of the alloys (in wt %).

Alloy Designation	Element (in wt %)						
	Mg	Zn	Fe	Gd	Nd	Y	Zr
Zn–2Mg	1.6	bal.	0.1	-	-	-	-
Mg–4Y–3RE	bal.	-	-	-	2.8	4.2	0.4

### 2.1. Structure and Mechanical Properties

The microstructures of the alloys were examined by optical (OM) and scanning electron microscopy (SEM, Tescan Vega 3, TESCANA Brno, s.r.o., Brno, Czech Republic) equipped with energy dispersion spectrometry (Oxford Instruments Aztec, Abingdon, UK). For this purpose, the samples were ground using SiC abrasive papers (P180–P4000), polished by diamond pastes with 2 and 0.7  $\mu\text{m}$  particles and etched in a 2 mL  $\text{HNO}_3$  + 100 mL  $\text{H}_2\text{O}$  solution. The phase composition of alloys was determined by X-ray diffraction (X'Pert Philips, Malvern, UK, 30 mA, 40 kV, X-ray radiation  $\text{Cu K}\alpha$ ). Mechanical properties of alloys were examined by tensile testing. Tensile tests were performed according to the  $\check{\text{C}}\text{SN EN ISO 6892-1}$  on cylindrical “dog bone” samples with 4 mm in diameter of gauge length (Figure 1). Tests were carried out on a LabTest 5.250SP1-VM universal loading machine (LABORTECH s.r.o., Opava, Czech Republic) at a deformation rate of 1 mm/min. Compressive tests were performed according to the ASTM E9–19 (Standard Test Methods of Compression Testing of Metallic Materials at Room Temperature). The cylindrical samples with 6 mm in diameter and 10 mm high were uniaxially compressed at a rate 1 mm/min. Both tensile and compressive tests were performed along to the extrusion direction.

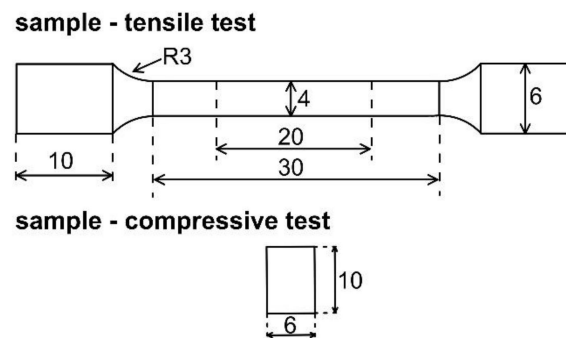


**Figure 1.** Shape of the samples for tensile and compressive test. All dimensions are in mm.

### 2.2. In Vitro Corrosion

The corrosion behaviour was studied in simulated body fluid (SBF27) prepared according to the Müller, et al. [45]. Both immersion tests and electrochemical potentiodynamic measurements were performed to assess corrosion resistance. In the former, valves 6 mm in diameter and 15 mm in thickness were immersed in SBF for 14 days at 37 °C. Afterwards, the corrosion products were removed by chemical agents according to ISO 8407. For the Zn-based alloys, these products were dissolved in a solution containing 200 g/L  $\text{CrO}_3$ . For the Mg–4Y–3RE alloy a solution of 200 g/L  $\text{CrO}_3$ , 10 g/L  $\text{AgNO}_3$  and 20 g/L  $\text{Ba}(\text{NO}_3)_2$  was used for this purpose. The corrosion rates were then calculated in mm/year using the weight losses measured on a balance with an accuracy of 0.1 mg, according to ASTM G31-72. The potentiodynamic curves of the alloys were measured in SBF at 37 °C (Gamry FAS1 potentiostat, Warminster, PA, USA). Experiments were performed in a standard three-electrode set-up: with the sample (a coupon 6 mm in diameter and 2 mm in thickness) as the working electrode, two graphite rods as the counter electrodes and  $\text{Ag}/\text{AgCl}/\text{KCl}$  (3 mol/L) as the reference electrode (SSCE) with a potential of 0.199 V/SHE. All potentials presented in this paper were measured against SSCE. Potentiodynamic curves were scanned from  $-0.2 \text{ V}/E_{\text{ocp}}$  to  $+0.5 \text{ V}/E_{\text{ocp}}$  at a rate of 2 mV/s. Before the measurement, the samples were stabilized in the solution for 30 min.

### 2.3. In Vivo Corrosion

For in vivo animal tests, the alloys were machined to hemispherical implants of 2.5 mm in diameter, see Figure 2. Ten male Wistar rats (Velaz, Prague, Czech Republic) were used as an experimental model. The animals were divided into two identical groups, one received the Mg–4Y–3RE implants and the other received the Zn–2Mg implants. The implants underwent sterilization by steam autoclaving

before implantation. The surgical procedure was conducted according to the university animal ethics committee. The animals were anaesthetized with 3% isoflurane (flow 300 mL/min) applied via face mask. After anaesthesia, the rats were placed into prone position and incision of the skin, subcutaneous soft tissues and periosteum were made. A hole of 2.5 mm in diameter was drilled into the bone between bregma and lambda with the use of a conventional device (W&H, SI-923, Austria, small diamond round bur, 10,000 rpm). One implant was placed into the bone defect in each rat (Figure 3). The bone cavity with the implant was then covered with periosteum, subcutaneous soft tissues and skin, sutured in layers with monofil. The rats were placed into each own cage and observed until completely recovered from anaesthesia. Postoperatively all rats were allowed to move freely, and each rat was housed alone in the cage to minimize postoperative damage of the wound. Rats were tested to evaluate motor and behavioural functions and CBCT (Cone Beam Computed Tomography) was used to observe possible gas formation. After a 12-week interval following implantation, the rats were euthanized, the implants were carefully extracted and subsequently analyzed. The corrosion products were removed firstly mechanically and subsequently by a water solution of 200 g/L CrO<sub>3</sub>, according to ISO 8407, and the corrosion rates were calculated from the weight losses, according to ASTM G31-72. The surface of corroded samples was analyzed using X-ray diffraction (XRD) (X-Pert Pro). To determine the chemical and phase compositions of corrosion products and assess the corrosion mechanisms of the alloys, the *in vivo* corroded samples were examined in cross-sections by a scanning electron microscope (SEM) Tescan Vega 3 and energy-dispersive spectrometer (EDS).

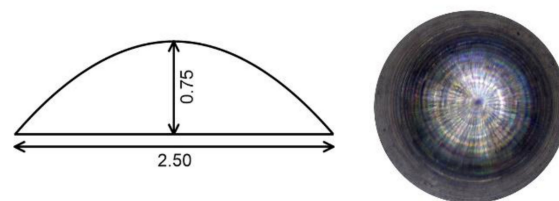


**Figure 2.** Hemispherical implants used in *in-vivo* animal testing. All dimensions are in mm.



**Figure 3.** Computed tomography (CT) image of the rat's cranium with the biodegradable implant.



### 3. Results

#### 3.1. Microstructure and Mechanical Properties

Microstructures and mechanical properties of the alloys are briefly summarized in Figure 4 and Table 2. The Zn–2Mg alloy is composed of dynamically recrystallized Zn phase with equiaxed grains of 10  $\mu\text{m}$  in size (measured on 100 grains by the line intercept method) appearing as light regions in Figure 4a. In this figure, there are also  $\text{Mg}_2\text{Zn}_{11}$  intermetallic phases (dark) arranged parallel to the hot extrusion direction. The morphology of eutectic particles is better seen on an SEM view of the etched sample in Figure 4c. It is obvious that eutectic lamellae typical for the as-cast state [49] are broken down and the eutectic mixture slightly coarsened during hot extrusion at a relatively high temperature.

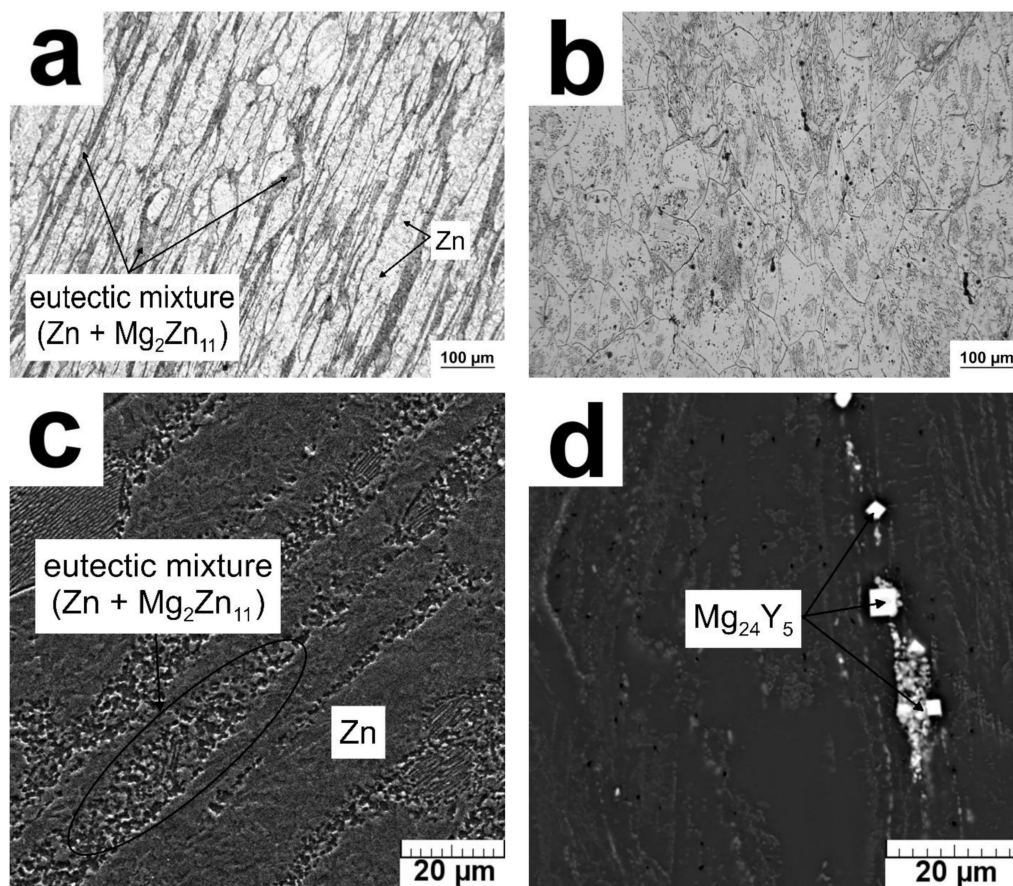


**Figure 4.** Microstructures of the examined alloys: (a) Zn–2Mg (OM), (b) Mg–4Y–3RE (OM), (c) Zn–2Mg (scanning electron microscope (SEM)), (d) Mg–4Y–3RE (SEM).

**Table 2.** Mechanical properties of the examined alloys (HV—Vickers Hardness, TYS—tensile yield strength at 0.2% offset, UTS—ultimate tensile strength, E—elongation, CYS—compressive yield strength at 0.2% offset, UCS—ultimate compressive strength).

Alloy	HV	TYS (MPa)	UTS (MPa)	E (%)	CYS (MPa)	UCS (MPa)
Zn–2Mg	97	235	365	4.9	231	426
Mg–4Y–3RE	114	280	316	5.3	239	402

The Mg–4Y–3RE alloy contains recrystallized slightly elongated grains of primary Mg in which major fractions of Y (3.8 wt %) and RE (3.2 wt %) are dissolved. The majority of intermetallic phases such as  $\text{Mg}_{14}\text{Nd}_2\text{Y}$  was dissolved during heat treatment at 525  $^\circ\text{C}/8$  h. Still, some Y-enriched  $\text{Mg}_{24}\text{Y}_5$

phase and  $\text{Mg}_{45.9}\text{Gd}_{9.08}$  were presented in the material based on the XRD results (Figure 5). This phase was observed also in literature [55] and its stoichiometry is close to  $\text{Mg}_5\text{Gd}$  [56,57]. Presented particles were arranged occasionally in the rows parallel to the extrusion direction (Figure 4d).

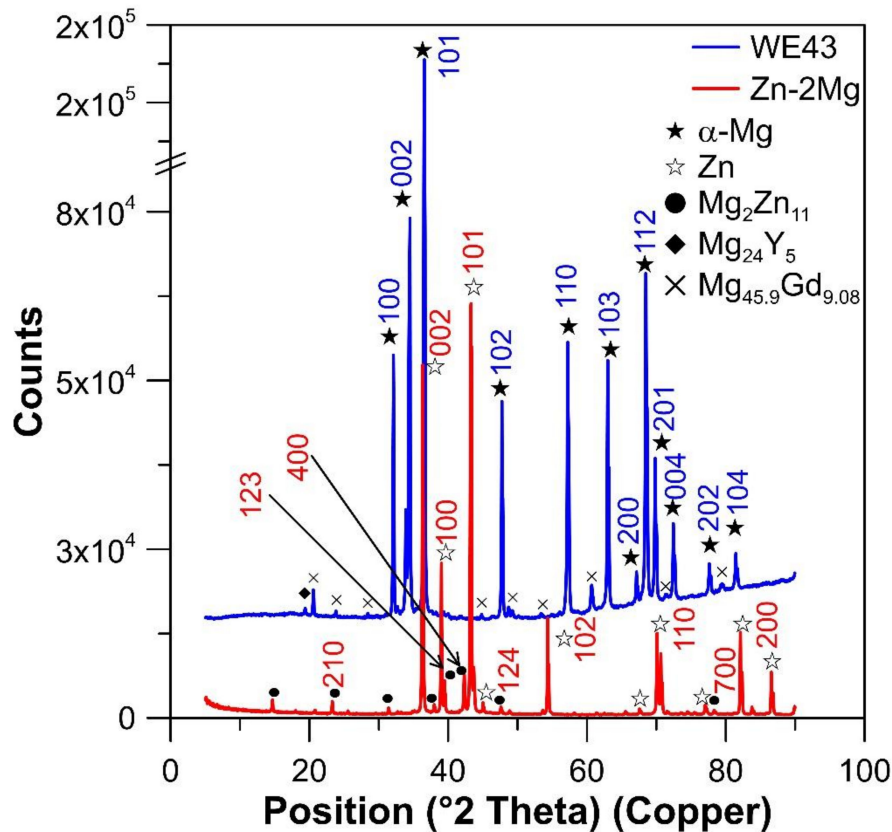


**Figure 5.** X-ray diffraction (XRD) of Zn-2Mg and Mg-4Y-3RE. Measured area is parallel to the extrusion direction. Subsequent powder diffraction patterns' ID have been used: Mg (00-001-1141),  $\text{Mg}_{24}\text{Y}_5$  (00-016-0854),  $\text{Gd}_{9.08}\text{Mg}_{45.9}$  (01-071-8824), Zn (00-001-1238),  $\text{Mg}_2\text{Zn}_{11}$  (04-007-1412). Numbers above the symbols reflect diffraction peaks of specific planes.

The stress–strain curves of studied materials both for compression and also tension loading are displayed in Figure 6. The values of mechanical properties are more clearly evident in Table 2. The existence of common fibre texture of the material with a hexagonal close-packed structure related to the extrusion with the majority of basal planes oriented parallel to the extrusion direction significantly affects the tensile yield strength (TYS) and compressive yield strength (CYS) values for tensile loading in the extrusion direction [58–61]. During tensile testing, materials are oriented inappropriately for basal slip and twinning and, therefore, higher stresses are necessary to activate more complicated slip and twinning mechanisms. As a consequence, the material seems to be more strengthened. However, if the same material is subjected to compressive tests in the direction of extrusion, the orientation is suitable for twinning and, therefore, the value of CYS is decreased compared to the value of TYS [58–61]. Based on the observed weak texture of Zn-2Mg alloy, values of CYS and TYS are very close and any significant anisotropy of mechanical properties has been observed. By contrast, a slight difference is evident for CYS and UTS in the case of Mg-4Y-3RE extruded alloy. However, the difference of 30 MPa is quite small and this suggests that texture strength is not strong. This is often observed in the case of magnesium-based alloys with RE elements in the structure because these elements suppress the formation of strong basal texture [61,62].

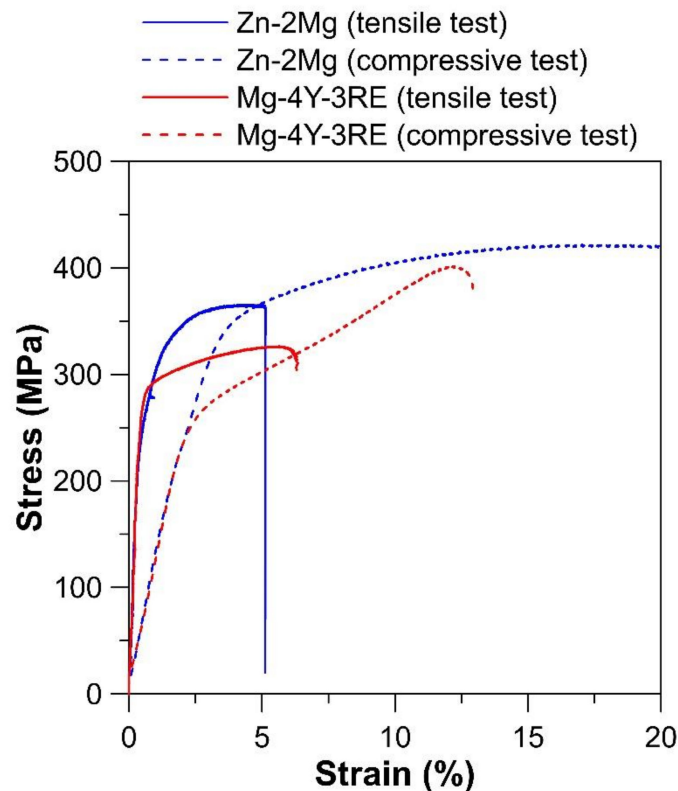


**Figure 6.** Stress–strain curves of Zn–2Mg and Mg–4Y–3RE alloys for compression and tensile loading.

Table 2 shows that the Zn–2Mg alloy exhibits a slightly lower hardness and yield strength, but a higher ultimate strength, than the Mg-based counterpart. However, it should be noted that both alloys fulfil the general mechanical requirements for metallic biodegradable implants (TYS > 200 MPa, UTS > 300 MPa) [28].

### 3.2. In Vitro Corrosion Behaviour

Figure 7 shows the potentiodynamic curves of the examined alloys in the SBF and Table 3 summarizes both in vitro electrochemical corrosion parameters and in vitro corrosion rates determined from weight losses of the alloys after exposition in SBF. As was expected, the potentiodynamic curve of the Zn–2Mg alloy is shifted to more noble potentials and lower current densities as compared to the Mg–4Y–3RE alloy (Figure 7). The difference between corrosion potentials of the alloys is 570 mV and that between corrosion current densities approximately one order of magnitude. In vitro corrosion rates of the Zn–2Mg and Mg–4Y–3RE alloys in the SBF calculated by using the Tafel extrapolation are 0.09 and 1.51 mm/year, respectively. The immersion tests confirmed superior corrosion resistance of the Zn–2Mg alloy compared to the Mg–4Y–3RE. Corrosion rates were determined as 0.09 and 0.50 mm/y for Mg–2Zn and Mg–4Y–3RE respectively. It is known that electrochemical methods in many cases provide different results of estimated corrosion rate compared to the classical weight changes measurements or hydrogen release for magnesium alloys. This is also seen in the present case, where the corrosion rate of the Mg–4Y–3RE alloy estimated from weight changes is threefold lower compared to the measurement by Tafel extrapolation. However, the potentiodynamic curves are measured at the beginning of exposure after one hour of stabilization in solution compared to the long immersion test performed for 42 days. The corrosion of magnesium is known to reduce after some time due to the protective character of the corrosion products formed. These products are in many cases composed of magnesium hydroxide, which is still partially soluble and porous. Therefore, deceleration of corrosion rate is in many cases connected with the formation of thicker corrosion product layer on magnesium, which takes some time. By contrast, on the surface of the zinc-based alloy, a thin protective surface



passive layer is formed very easily and quickly. Consequently, estimation of corrosion rate from Tafel slopes after 1 h provides the comparable result as weight changes after a significantly prolonged time of exposure.

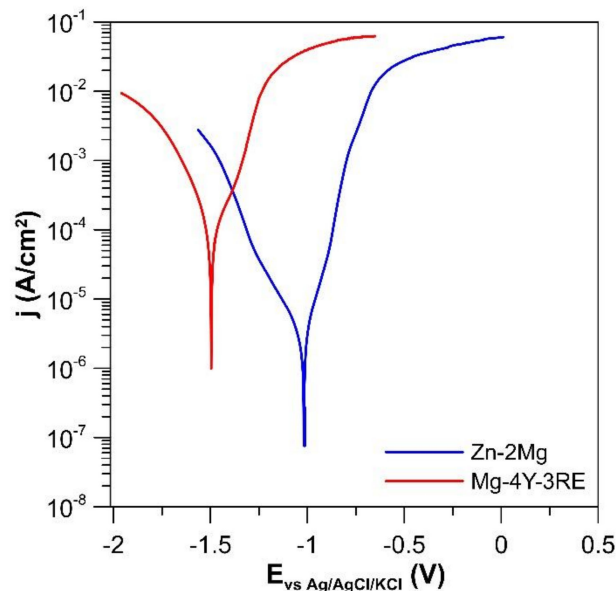


**Figure 7.** Potentiodynamic curves of the examined alloys in the simulated body fluid (SBF).

**Table 3.** Electrochemical corrosion parameters (corrosion potential  $E_{cor}$ , corrosion current density  $j_{cor}$ ) and corrosion rates  $v_{cor}$  of the examined alloys.

<i>In Vitro Tests</i>				
Alloy	$E_{cor}$ (mV/SSCE)	$j_{cor}$ (A/cm <sup>2</sup> )	$v_{cor\_PD}$ Curves (mm/year)	$v_{cor\_Weight}$ Changes (mm/year)
Zn-2Mg	-980	$6 \times 10^{-6}$	0.09	$0.091 \pm 0.018$
Mg-4Y-3RE	-1550	$7 \times 10^{-5}$	1.51	$0.495 \pm 0.128$

Surfaces of samples after immersion tests are displayed in Figure 8. Global chemical composition based on EDS analysis is shown in Table 4. Both alloys are covered by corrosion products composed of oxides and phosphates. The corrosion products on magnesium alloy are predominantly composed of magnesium hydroxide, which is precipitated on the surface and creates massive corrosion products. This is supplemented by magnesium doped calcium phosphate. In the case of Zn-2Mg, the surface is enriched by oxygen, phosphorus and calcium, which confirm the precipitation of mixed hydrated oxides, chlorides, phosphates and carbonates. The bigger difference between both studied materials is evident after removing corrosion products (Figure 8b,d). Magnesium alloy is in this case locally attacked. On the contrary, the surface of zinc alloy is attacked faintly compared to the Mg-4Y-3RE. This behaviour clearly illustrates the observed differences in corrosion rates.

**Table 4.** Chemical composition (in wt %) of corrosion products after immersion tests in SBF.

Alloy Designation	O	Mg	Zn	P	Ca	Y	Nd	Gd	Dy
Mg-4Y-3RE	43.3	48.2	-	3.2	3.6	1.3	0.4	-	-
Zn-2Mg	23.1	0.3	55.9	10.7	10.3	-	-	-	-

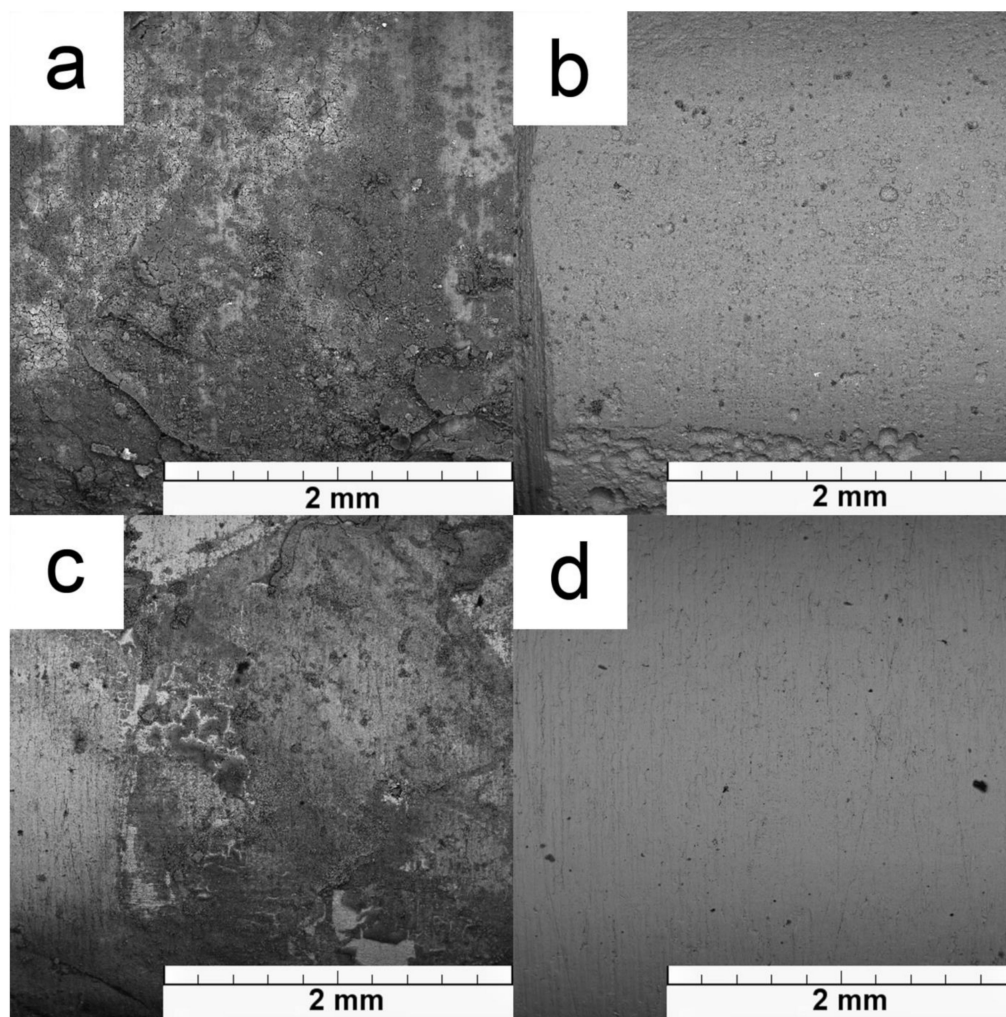


**Figure 8.** The surface of samples after in-vitro corrosion tests before (a,c) and after (b,d) removing of corrosion products: (a,b) Mg-4Y-3RE, (c,d) Zn-2Mg.

### 3.3. In Vivo Corrosion and Biocompatibility

Although the biocompatibility assessment was not the main task of this study, visual observation of the living animals and inspection of implant location 12 weeks after implantation was performed. These tests show that the biodegradable Zn and Mg-based implants have no adverse effects on the behaviour or physical condition of rats. Moreover, gas bubbles and inflammatory reaction of the living tissue were not detected after 12 weeks period.

Based on the weight changes, in vivo corrosion rates were established as 0.10 and 0.90 mm/year for the Zn-2Mg and Mg-4Y-3RE alloys, respectively. This is in a relatively good agreement with the in-vitro tests. The overall views of the cross-sectioned samples after 12-week in vivo corrosion are shown in Figure 9. It is observed in Figure 9a that the Zn-2Mg alloy retains the round shape after in-vivo exposition suggesting relatively slow and uniform corrosion. In contrast, the reference Mg-4Y-3RE alloy (Figure 8b) shows an irregular shape and thicker corrosion products confirming a higher in vivo corrosion rate of this alloy.

X-ray elemental mapping and point EDS microanalysis (except for C) were performed in selected regions to study corrosion products covering the alloys. Figure 10 and Table 5 characterize the Zn-2Mg alloy. It is obvious that corrosion products consist of at least two constituents: The first one (lighter in Figure 10) has higher Zn and O concentrations and lower P and Ca concentrations (points 1–4 in Table 5). The second component of the corrosion layer (darker in Figure 10) contains, besides Zn and O, enhanced concentrations of Ca and P (points 5–7 in Table 5). Besides, traces of Cl are detected in

corrosion products covering the zinc alloy. It can be assumed that the first component of the corrosion layer is dominated by ZnO (or a mixture of ZnO + ZnCO<sub>3</sub>) while the second contains a mixed calcium zinc phosphate (Zn, Ca)<sub>3</sub>(PO<sub>4</sub>)<sub>2</sub>.

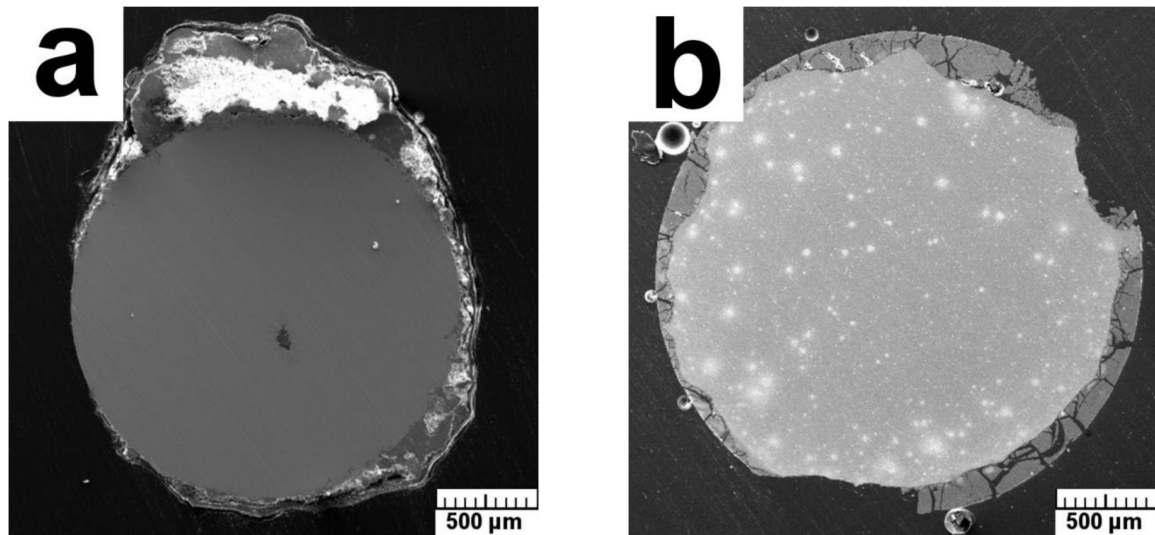


**Figure 9.** The overall views of the cross-sectioned samples after 12-week in vivo corrosion: (a) the Zn-2Mg alloy, (b) the Mg-4Y-3RE alloy.

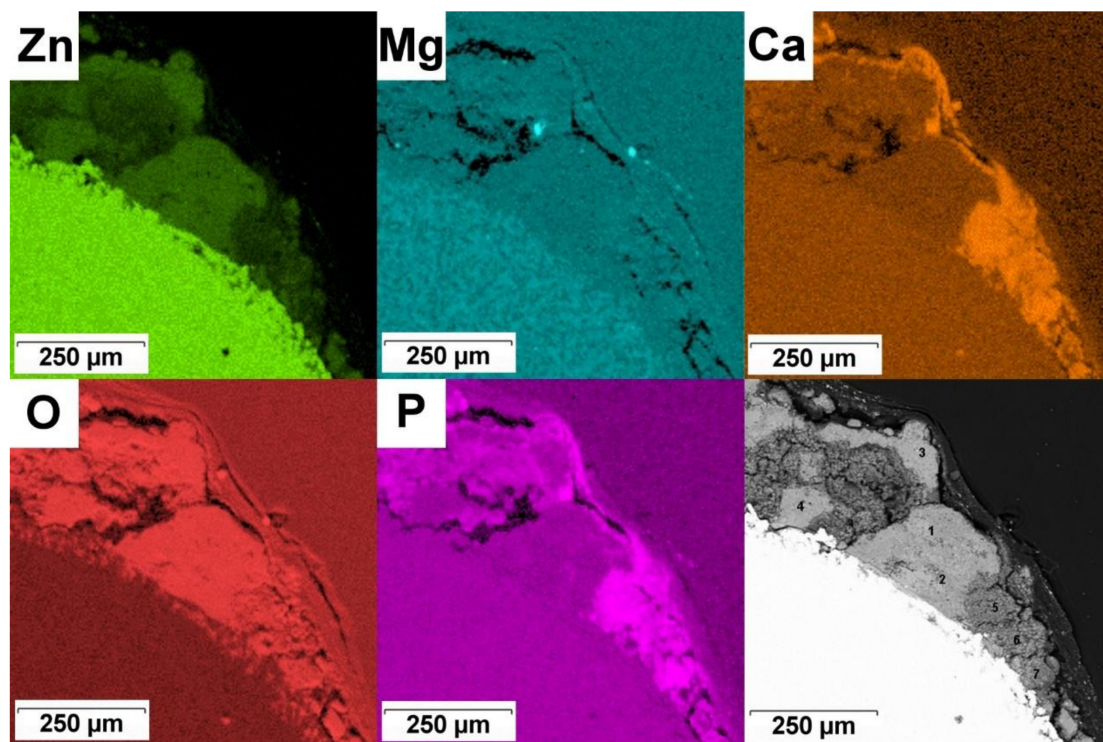


**Figure 10.** Corrosion products on the in-vivo corroded Zn-2Mg alloy and corresponding elemental maps.

Elemental composition of corrosion products on the Mg alloy is presented in X-ray maps in Figure 11. As in the previous case, corrosion products mainly contain Mg, O, P and Ca (light carbon was not measured). These elements are not distributed uniformly as P and Ca are enriched in external parts of the corrosion layer. The main corrosion products of the Mg-4Y-3RE alloy are thus Mg(OH)<sub>2</sub>,



MgCO<sub>3</sub> and (Mg, Ca)<sub>3</sub>(PO<sub>4</sub>)<sub>2</sub> which is in accordance with observations of other authors [53,63,64]. Rare earth metals partially substitute magnesium and calcium in these compounds.

**Table 5.** Chemical compositions (in wt %) of corrosion products at points depicted in Figure 9 (C is not included).

Point	O	Mg	P	Cl	Ca	Zn
1	20.8	-	0.4	0.6	-	78.2
2	23.9	-	0.3	0.3	0.3	75.2
3	19.3	-	0.5	1.2	-	79.0
4	21.3	-	-	1.0	-	77.7
5	28.9	0.4	12.9	0.6	11.9	45.3
6	18.9	0.3	8.9	0.4	10.2	61.3
7	35.3	0.6	10.6	0.2	8.2	45.1

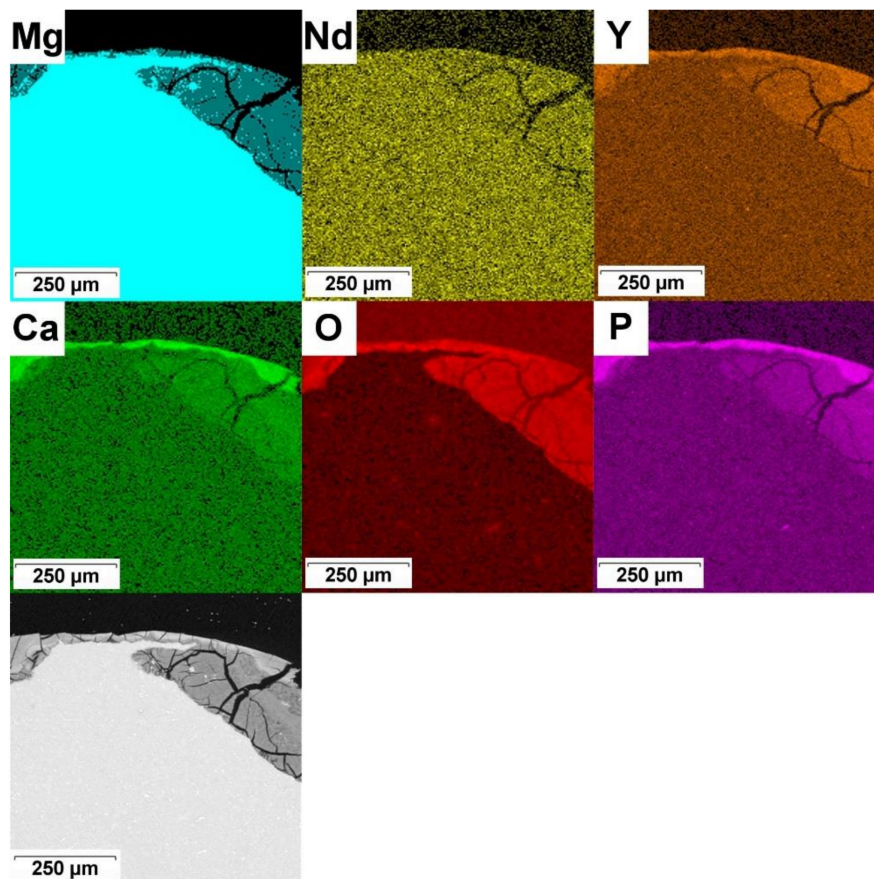


**Figure 11.** Corrosion products on the in vivo corroded Mg-4Y-3RE alloy and corresponding elemental maps.

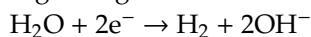
#### 4. Discussion

Tensile mechanical properties of extruded Zn-2Mg alloy were determined as 235 MPa for TYS and 265 MPa for UTS. These values are significantly higher compared to the 200 and 270 MPa determined in the case of extruded Zn-1Mg alloy by Li et al. [33]. Gong et al. [32] measured mechanical properties of extruded Zn-1Mg and achieved the values about 180 MPa for TYS and 250 MPa for UTS with elongation of 10%. Increased mechanical properties in the present study are related especially to the increased amount of Mg in the alloy and, therefore, strengthening by secondary phases which

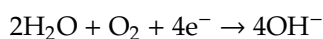
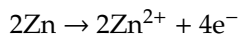
are presented in the microstructure. Strengthening by grain boundaries described by the Hall–Petch relation is another well-known strengthening mechanism. However, the grain size of all compared materials was close to 10  $\mu\text{m}$ . A solution strengthening mechanism is not considered because solid solubility of Mg in Zn is negligible and the texture contribution effect is considered to be very low in the present state due to the low texture strength. Regarding mechanical properties, modulus of elasticity has an important role especially for applications like fixation devices. The low value of modulus of elasticity of magnesium-based materials ( $\approx 45$  GPa) is relatively close to the general value of natural bones ( $\approx 20$ – $25$  GPa), which partially suppress the stress-shielding effect. This effect is connected to the non-uniform distribution of loading on implant and healing bone. The rough value of modulus of elasticity ( $\approx 90$  MPa) obtained for Zn–2Mg from tensile curve indicate that combining these materials with bone may lead to greater susceptibility to the stress shielding effect.

Corrosion behaviour of this alloy was compared with well-known biodegradable Mg-based alloy Mg–4Y–3RE. Both measurements have shown that zinc alloy corrodes relatively slowly and uniformly. Comparing the corrosion rates of Zn–2Mg and Mg–4Y–3RE calculated from weight losses, it can be seen easily that Zn–2Mg alloy degrades in in vitro and in vivo conditions 5 or 9 times slower, respectively. This is due to several differences in the corrosion behaviour of zinc and magnesium.

For Mg, anodic and cathodic reactions following can be written [65]:

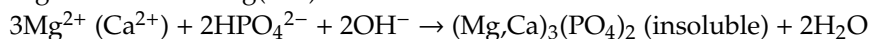
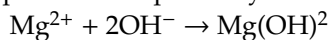


Corrosion mechanism for Zn can be described as [65]:



While magnesium is not sensitive to the oxygen present in the corrosion medium, the cathodic reaction for zinc involves the reduction of oxygen. Therefore, there is nearly no evolution of hydrogen during zinc corrosion. This is important not only in terms of corrosion rate but also in terms of the healing process.

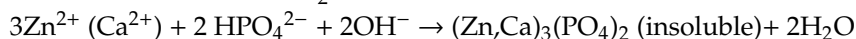
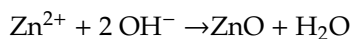
Released cations and  $\text{OH}^{-}$  anions take place in reactions with different components of the medium in which the samples are exposed and form corrosion products. In the case of Mg–4Y–3RE, the considered corrosion products were  $\text{Mg}(\text{OH})_2$ ,  $(\text{Mg}, \text{Ca})_3(\text{PO}_4)_2$  and  $\text{MgCO}_3$ . Formation of these compounds is depicted by the following equations:



Based on the XRD measurements (Figure 12) of the corrosion product on samples from in vivo tests, only  $\text{Mg}(\text{OH})_2$  was formed as the main component of corrosion products. The presence of NaCl in Figure 12 is not related to the formation of this product during the in vivo test. Instead, it was crystallized from residual solution probably in some crack between corrosion products after removing the sample from animal, washing the sample and drying it. The same information can be obtained from Figure 11, where huge areas containing Mg, O and partially Y are evident. There also exists a thin layer of calcium, magnesium mixture phosphate, which, due to its low thickness, could not be identified by XRD (Figure 12). It seems that during the corrosion process, pH at the surface is increased early and magnesium calcium phosphates precipitate at the surface. This layer forms a barrier but still the corrosion process continues under it to form predominantly  $\text{Mg}(\text{OH})_2$  or  $\text{MgCO}_3$ .

In the corrosion layer on Zn–2Mg samples, ZnO or its hydrated forms, mixed calcium-zinc phosphate and also zinc carbonate are formed. Although EDS microanalysis does not provide accurate values for C, the aforementioned products were confirmed after the immersion test by XRD (Figure 12).

Reactions of zinc cation with the surrounding medium yielding corrosion products are:





Although both Zn and Ca partially occupy the surface phosphate layer, the dominant cation is  $\text{Ca}^{2+}$ . Therefore, it seems that zinc-based corrosion products are especially carbonates and mixed hydrated oxides and chlorides (Figure 12). Standard potentials of Mg and Zn are  $-2.372$  and  $-0.762$  V, respectively [36], which are very distinctive values. Slower corrosion concerning Zn-based alloys as more noble material is thus partially connected with higher corrosion potential ( $-0.98$  V vs.  $-1.55$  V for Mg-4Y-3RE, Figure 7, Table 3). Also, high hydrogen overpotential of Zn has an important influence on the corrosion rate. Due to the high overpotential, the evolution of hydrogen on the surface of zinc is suppressed. Consequently, the cathodic reaction is dominated by the reduction of dissolved oxygen and this process is controlled by diffusion, which leads to a limitation of cathodic current. This phenomenon was affirmed by measurement of potentiodynamic curves.

Although the differences in the corrosion rate of magnesium alloy in vivo and in vitro are evident and this observation is very well-known, there is a very good similarity between the corrosion rates of the Zn-2Mg alloy in both conditions. Also, the corrosion products were composed of the same constituents, however, it is necessary to mention, that participation of some organic elements in the corrosion process in-vivo is not considered which can be the reason for increased corrosion rate of Mg-4Y-3RE.

The in vitro corrosion rate of the Zn-2Mg alloy has been also determined in other papers [32,33,35]. Gong et al. [32] determined the corrosion rate of the Zn-1Mg alloy in SBF as  $0.12$  mm/y, which is very close to the observed values. Li et al. [33] calculated corrosion rates of Zn-1Mg immersed in Hank's solution as  $0.15$  mm/y from Tafel slopes and  $0.08$  mm/y from weight changes. This is also close in value to the  $0.09$  mm/y assessed in our case. Some difference can be connected with the choice of different modelling environment for the immersion tests.

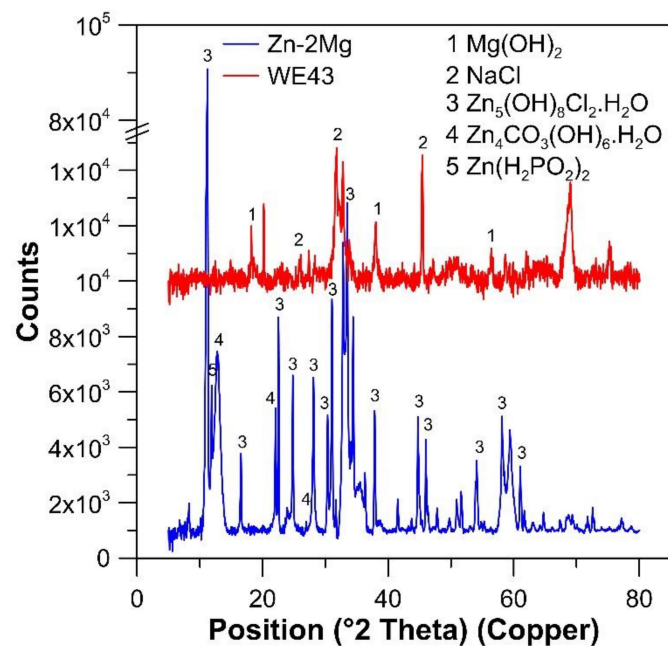


**Figure 12.** X-ray diffraction of the surfaces of Zn-2Mg and Mg-4Y-3RE after in vivo tests. Subsequent powder diffraction pattern IDs have been used:  $\text{Mg}(\text{OH})_2$  (00-001-1169),  $\text{NaCl}$  (00-001-0993),  $\text{Zn}_5(\text{OH})_8\text{Cl}_2 \cdot \text{H}_2\text{O}$  (00-007-0155),  $\text{Zn}_4\text{CO}_3(\text{OH})_6 \cdot \text{H}_2\text{O}$  (00-003-0787),  $\text{Zn}(\text{H}_2\text{PO}_2)_2$  (04-010-4355).

Our earlier studies showed that corrosion rates of Zn-Mg alloy with 0.5–2 wt % of Mg are a very similar and only slight trend in the improvement of corrosion resistance with the increased amount of Mg has been observed [35,49]. This can be also the reason for the slightly decreased corrosion rate of the presented Zn-2Mg alloy that was observed.

The corrosion rate of Zn-2Mg alloy estimated from in vivo tests was determined as  $0.1$  mm/year. Li et al. [33] determined the in vitro corrosion rate of Zn-1Mg alloy by micro-CT analysis as  $0.17$  mm/y.

Some difference in corrosion rates can be connected with different methodology but both these values are very promising. To establish if the requirements for biocompatibility are accommodated, one can visualize a real application, such as a screw for bone fixation. The bone screw is often fabricated with average dimensions about 30 mm in length and 3 mm in diameter. By simplified calculation, with an assumption of uniform corrosion at a rate of 0.1 mm/year, one obtains that 1 mg of Zn per day is released into the organism. Such an amount is significantly lower than the upper recommended daily limit representing 40 mg of Zn. This implies that the use of zinc alloyed by a small percentage of magnesium remains non-toxic during its use in the form of a small bone-fixation device.

Apart from biocompatibility, biodegradable materials for load-bearing applications also require feasible mechanical performance during the healing process. From the surgical point of view, a fixation screw should preserve at least 95% of its original load-bearing capability during the first 6 weeks after implantation. This means that the screw can undergo such corrosion so that its cross-section would reduce by less than 5%. This requirement gives a maximum acceptable corrosion rate of 0.4 mm/year. Therefore, it can be seen that in the case of the investigated Zn–2Mg alloy, this requirement is satisfied. For the reference Mg–4Y–3RE alloy, the corrosion rate of 0.9 mm/year already exceeds this limit.

## 5. Conclusions

The present paper deals with the study of the microstructure, mechanical and corrosion behaviour of Zn–2Mg and Mg–4Y–3RE alloys. Yield strength and ultimate strength of Zn–2Mg in tension and compression exceed 230 and 360 MPa, respectively, which are considered as sufficient values to ensure mechanical support for healed bone during the regeneration process. Moreover, uniform degradation and low corrosion rates of Zn–2Mg determined both in vitro (0.09 mm/year) and in vivo (0.10 mm/year) fulfil general requirements to ensure sufficient mechanical integrity and low doses of released ions into the human organism during implant degradation. Good biocompatibility of Zn–2Mg was stated based on no adverse effects on the behaviour or physical condition of rats and no inflammatory reaction of the living tissue observed after 12 weeks period of in vivo tests. All these findings demonstrate that the zinc-based alloy Zn–2Mg prepared by conventional casting and hot extrusion process meet the key requirements for load-bearing biodegradable implant application like fixation devices (screws and plates). Although yield strength and ultimate strength of Zn–2Mg and Mg–4Y–3RE are almost similar, the in vivo corrosion rate of Zn–2Mg is nine times lower and the biodegradation is not accompanied by hydrogen release. However, such an advantage over Mg–4Y–3RE is partially negated by low ductility ( $\approx 5\%$ ) and a higher value of modulus of elasticity ( $\approx 90$  GPa). Therefore, none of the studied materials is superior and individual alloys may be preferred for specific conditions.

**Author Contributions:** Conceptualization, J.K. and D.V.; methodology, D.D. and J.Š.; validation, D.V. and R.F.; investigation, J.K., D.D., Š.M., J.L. and J.Š.; writing—J.K. and J.L.; writing—review and editing, D.V. and R.F.; supervision, D.V.

**Funding:** This research was funded by The Czech Science Foundation (project no. 18-06110S) and specific university research (MSMT no. 21/2019).

**Conflicts of Interest:** The authors declare no conflict of interest.

## References

1. Smith, P.; Kirkland, N.T.; Birbilis, N. Introduction to Magnesium Biomaterials. In *Magnesium Biomaterials: Design, Testing, and Best Practice*; Springer International Publishing: Heidelberg, Germany, 2014; pp. 1–12. [[CrossRef](#)]
2. Purnama, A.; Hermawan, H.; Mantovani, D. Biodegradable Metal Stents: A Focused Review on Materials and Clinical Studies. *J. Biomater. Tissue Eng.* **2014**, *4*, 868–874. [[CrossRef](#)]
3. Manivasagam, G.; Suwas, S. Biodegradable Mg and Mg based alloys for biomedical implants. *Mater. Sci. Technol.* **2014**, *30*, 515–520. [[CrossRef](#)]
4. Chen, Y.J.; Xu, Z.G.; Smith, C.; Sankar, J. Recent advances on the development of magnesium alloys for biodegradable implants. *Acta Biomater.* **2014**, *10*, 4561–4573. [[CrossRef](#)]

5. Gu, X.N.; Li, S.S.; Li, X.M.; Fan, Y.B. Magnesium based degradable biomaterials: A review. *Front. Mater. Sci.* **2014**, *8*, 200–218. [[CrossRef](#)]
6. Ding, Y.F.; Wen, C.E.; Hodgson, P.; Li, Y.C. Effects of alloying elements on the corrosion behavior and biocompatibility of biodegradable magnesium alloys: A review. *J. Mater. Chem. B* **2014**, *2*, 1912–1933. [[CrossRef](#)]
7. Waizy, H.; Seitz, J.-M.; Reifenrath, J.; Weizbauer, A.; Bach, F.-W.; Meyer-Lindenberg, A.; Denkena, B.; Windhagen, H. Biodegradable magnesium implants for orthopedic applications. *J. Mater. Sci.* **2013**, *48*, 39–50. [[CrossRef](#)]
8. Tan, L.L.; Yu, X.M.; Wan, P.; Yang, K. Biodegradable Materials for Bone Repairs: A Review. *J. Mater. Sci. Technol.* **2013**, *29*, 503–513. [[CrossRef](#)]
9. Persaud-Sharma, D.; McGoron, A. Biodegradable Magnesium Alloys: A Review of Material Development and Applications. *J. Biomim. Biomater. Tissue Eng.* **2012**, *12*, 25–39. [[CrossRef](#)]
10. Virtanen, S. Biodegradable Mg and Mg alloys: Corrosion and biocompatibility. *Mater. Sci. Eng. B Adv.* **2011**, *176*, 1600–1608. [[CrossRef](#)]
11. Atrens, A.; Liu, M.; Zainal Abidin, N.I. Corrosion mechanism applicable to biodegradable magnesium implants. *Mater. Sci. Eng. B* **2011**, *176*, 1609–1636. [[CrossRef](#)]
12. Witte, F. The history of biodegradable magnesium implants: A review. *Acta Biomater.* **2010**, *6*, 1680–1692. [[CrossRef](#)] [[PubMed](#)]
13. Syntellix. Available online: <https://www.syntellix.de/en/products/product-overview/all.html> (accessed on 2 October 2019).
14. Wegener, B.; Sievers, B.; Utschneider, S.; Muller, P.; Jansson, V.; Rossler, S.; Nies, B.; Stephani, G.; Kieback, B.; Quadbeck, P. Microstructure, cytotoxicity and corrosion of powder-metallurgical iron alloys for biodegradable bone replacement materials. *Mater. Sci. Eng. B Adv.* **2011**, *176*, 1789–1796. [[CrossRef](#)]
15. Cheng, J.; Liu, B.; Wu, Y.H.; Zheng, Y.F. Comparative in vitro Study on Pure Metals (Fe, Mn, Mg, Zn and W) as Biodegradable Metals. *J. Mater. Sci. Technol.* **2013**, *29*, 619–627. [[CrossRef](#)]
16. Francis, A.; Yang, Y.; Virtanen, S.; Boccaccini, A.R. Iron and iron-based alloys for temporary cardiovascular applications. *J. Mater. Sci. Mater. Med.* **2015**, *26*, 138. [[CrossRef](#)]
17. Liu, B.; Zheng, Y.F. Effects of alloying elements (Mn, Co, Al, W, Sn, B, C and S) on biodegradability and in vitro biocompatibility of pure iron. *Acta Biomater.* **2011**, *7*, 1407–1420. [[CrossRef](#)] [[PubMed](#)]
18. Liu, B.; Zheng, Y.F.; Ruan, L. In vitro investigation of Fe<sub>30</sub>Mn<sub>6</sub>Si shape memory alloy as potential biodegradable metallic material. *Mater. Lett.* **2011**, *65*, 540–543. [[CrossRef](#)]
19. Schinhammer, M.; Steiger, P.; Moszner, F.; Löffler, J.F.; Uggowitz, P.J. Degradation performance of biodegradable FeMnC(Pd) alloys. *Mater. Sci. Eng. C* **2013**, *33*, 1882–1893. [[CrossRef](#)]
20. Hermawan, H.; Purnama, A.; Dube, D.; Couet, J.; Mantovani, D. Fe–Mn alloys for metallic biodegradable stents: Degradation and cell viability studies. *Acta Biomater.* **2010**, *6*, 1852–1860. [[CrossRef](#)]
21. Peuster, M.; Wohlsein, P.; Brugmann, M.; Ehlerding, M.; Seidler, K.; Fink, C.; Brauer, H.; Fischer, A.; Hausdorf, G. A novel approach to temporary stenting: Degradable cardiovascular stents produced from corrodible metal—Results 6–18 months after implantation into New Zealand white rabbits. *Heart* **2001**, *86*, 563–569. [[CrossRef](#)]
22. Peuster, M.; Hesse, C.; Schloo, T.; Fink, C.; Beerbaum, P.; von Schnakenburg, C. Long-term biocompatibility of a corrodible peripheral iron stent in the porcine descending aorta. *Biomaterials* **2006**, *27*, 4955–4962. [[CrossRef](#)]
23. Moravej, M.; Mantovani, D. Biodegradable Metals for Cardiovascular Stent Application: Interests and New Opportunities. *Int. J. Mol. Sci.* **2011**, *12*, 4250–4270. [[CrossRef](#)] [[PubMed](#)]
24. Wu, C.; Hu, X.Y.; Qiu, H.; Ruan, Y.M.; Tang, Y.; Wu, A.L.; Tian, Y.; Peng, P.; Chu, Y.; Xu, X.L.; et al. A Preliminary Study of Biodegradable Iron Stent in Mini-Swine Coronary Artery. *J. Am. Coll. Cardiol.* **2012**, *60*, B166. [[CrossRef](#)]
25. Waksman, R.O.N.; Pakala, R.; Baffour, R.; Seabron, R.; Hellinga, D.; Tio, F.O. Short-Term Effects of Biocorrodible Iron Stents in Porcine Coronary Arteries. *J. Interv. Cardiol.* **2008**, *21*, 15–20. [[CrossRef](#)] [[PubMed](#)]
26. Mueller, P.P.; Arnold, S.; Badar, M.; Bormann, D.; Bach, F.W.; Drynda, A.; Meyer-Lindenberg, A.; Hauser, H.; Peuster, M. Histological and molecular evaluation of iron as degradable medical implant material in a murine animal model. *J. Biomed. Mater. Res. A* **2012**, *100*, 2881–2889. [[CrossRef](#)]
27. Zheng, Y.F.; Gu, X.N.; Witte, F. Biodegradable metals. *Mater. Sci. Eng. R Rep.* **2014**, *77*, 1–34. [[CrossRef](#)]

28. Bowen, P.K.; Drelich, J.; Goldman, J. Zinc Exhibits Ideal Physiological Corrosion Behavior for Bioabsorbable Stents. *Adv. Mater.* **2013**, *25*, 2577–2582. [[CrossRef](#)]
29. Kubasek, J.; Vojtech, D.; Tanger, L.T.D. *Zn-Based Alloys as an Alternative Biodegradable Materials*; Tanger Ltd.: Slezska, Czech Republic, 2012; pp. 1355–1361.
30. Murni, N.S.; Dambatta, M.S.; Yeap, S.K.; Froemming, G.R.A.; Hermawan, H. Cytotoxicity evaluation of biodegradable Zn-3Mg alloy toward normal human osteoblast cells. *Mater. Sci. Eng. C Mater.* **2015**, *49*, 560–566. [[CrossRef](#)]
31. Dambatta, M.; Murni, N.; Izman, S.; Kurniawan, D.; Froemming, G.; Hermawan, H. In vitro degradation and cell viability assessment of Zn-3Mg alloy for biodegradable bone implants. *Proc. Inst. Mech. Eng. Part H J. Eng. Med.* **2015**, *229*, 335–342. [[CrossRef](#)]
32. Gong, H.; Wang, K.; Strich, R.; Zhou, J.G. In vitro biodegradation behavior, mechanical properties, and cytotoxicity of biodegradable Zn-Mg alloy. *J. Biomed. Mater. Res. Part B Appl. Biomater.* **2015**, *103*, 1632–1640. [[CrossRef](#)]
33. Li, H.F.; Xie, X.H.; Zheng, Y.F.; Cong, Y.; Zhou, F.Y.; Qiu, K.J.; Wang, X.; Chen, S.H.; Huang, L.; Tian, L.; et al. Development of biodegradable Zn-1X binary alloys with nutrient alloying elements Mg, Ca and Sr. *Sci. Rep.* **2015**, *5*, 10719. [[CrossRef](#)]
34. Liu, X.W.; Sun, J.K.; Yang, Y.H.; Pu, Z.J.; Zheng, Y.F. In vitro investigation of ultra-pure Zn and its mini-tube as potential bioabsorbable stent material. *Mater. Lett.* **2015**, *161*, 53–56. [[CrossRef](#)]
35. Kubasek, J.; Vojtech, D.; Jablonska, E.; Pospisilova, I.; Lipov, J.; Ruml, T. Structure, mechanical characteristics and in vitro degradation, cytotoxicity, genotoxicity and mutagenicity of novel biodegradable Zn-Mg alloys. *Mater. Sci. Eng. C Mater.* **2016**, *58*, 24–35. [[CrossRef](#)] [[PubMed](#)]
36. Vojtech, D.; Kubasek, J.; Serak, J.; Novak, P. Mechanical and corrosion properties of newly developed biodegradable Zn-based alloys for bone fixation. *Acta Biomater.* **2011**, *7*, 3515–3522. [[CrossRef](#)] [[PubMed](#)]
37. Fosmire, G.J. Zinc Toxicity. *Am. J. Clin. Nutr.* **1990**, *51*, 225–227. [[CrossRef](#)]
38. Wang, H.; Shi, Z.M.; Yang, K. Magnesium and magnesium alloys as degradable metallic biomaterials. In Proceedings of the 4th International Light Metals Technology Biennial Conference (LMT2009), Gold Coast, QLD, Australia, 29 June–1 July 2009; pp. 207–210.
39. Zberg, B.; Uggowitz, P.J.; Loffler, J.F. MgZnCa glasses without clinically observable hydrogen evolution for biodegradable implants. *Nat. Mater.* **2009**, *8*, 887–891. [[CrossRef](#)]
40. Bowen, P.K.; Guillory, R.J.; Shearier, E.R.; Seitz, J.-M.; Drelich, J.; Bocks, M.; Zhao, F.; Goldman, J. Metallic zinc exhibits optimal biocompatibility for bioabsorbable endovascular stents. *Mater. Sci. Eng. C* **2015**, *56*, 467–472. [[CrossRef](#)]
41. Zhao, S.; Seitz, J.-M.; Eifler, R.; Maier, H.J.; Guillory, R.J.; Earley, E.J.; Drelich, A.; Goldman, J.; Drelich, J.W. Zn-Li alloy after extrusion and drawing: Structural, mechanical characterization, and biodegradation in abdominal aorta of rat. *Mater. Sci. Eng. C* **2017**, *76*, 301–312. [[CrossRef](#)]
42. Bowen, P.K.; Seitz, J.M.; Guillory, R.J.; 2nd; Braykovich, J.P.; Zhao, S.; Goldman, J.; Drelich, J.W. Evaluation of wrought Zn-Al alloys (1, 3, and 5 wt % Al) through mechanical and in vivo testing for stent applications. *J. Biomed. Mater. Res. Part. B Appl. Biomater.* **2018**, *106*, 245–258. [[CrossRef](#)]
43. Yang, H.; Wang, C.; Liu, C.; Chen, H.; Wu, Y.; Han, J.; Jia, Z.; Lin, W.; Zhang, D.; Li, W.; et al. Evolution of the degradation mechanism of pure zinc stent in the one-year study of rabbit abdominal aorta model. *Biomaterials* **2017**, *145*, 92–105. [[CrossRef](#)]
44. Katarivas Levy, G.; Goldman, J.; Aghion, E. The Prospects of Zinc as a Structural Material for Biodegradable Implants—A Review Paper. *Metals* **2017**, *7*, 402. [[CrossRef](#)]
45. Bowen, P.K.; Shearier, E.R.; Zhao, S.; Guillory, R.J.; Zhao, F.; Goldman, J.; Drelich, J.W. Biodegradable Metals for Cardiovascular Stents: From Clinical Concerns to Recent Zn-Alloys. *Adv. Healthc. Mater.* **2016**, *5*, 1121–1140. [[CrossRef](#)] [[PubMed](#)]
46. Seitz, J.M.; Durisin, M.; Goldman, J.; Drelich, J.W. Recent Advances in Biodegradable Metals for Medical Sutures: A Critical Review. *Adv. Healthc. Mater.* **2015**, *4*, 1915–1936. [[CrossRef](#)] [[PubMed](#)]
47. Mostaed, E.; Sikora-Jasinska, M.; Drelich, J.W.; Vedani, M. Zinc-based alloys for degradable vascular stent applications. *Acta Biomater.* **2018**, *71*, 1–23. [[CrossRef](#)] [[PubMed](#)]
48. Venezuela, J.; Dargusch, M.S. The influence of alloying and fabrication techniques on the mechanical properties, biodegradability and biocompatibility of zinc: A comprehensive review. *Acta Biomater.* **2019**, *87*, 1–40. [[CrossRef](#)]

49. Kubasek, J.; Pospisilova, I.; Vojtech, D.; Jablonska, E.; Ruml, T. Structural, mechanical and cytotoxicity characterization of as-cast biodegradable Zn-xMg ( $x = 0.8\text{--}8.3\%$ ) alloys. *Mater. Tehnol.* **2014**, *48*, 623–629.
50. Gu, X.; Zheng, Y.; Zhong, S.; Xi, T.; Wang, J.; Wang, W. Corrosion of, and cellular responses to Mg–Zn–Ca bulk metallic glasses. *Biomaterials* **2010**, *31*, 1093–1103. [[CrossRef](#)]
51. Pan, F.; Bai, S.-L.; Zhang, E.-L.; Yu, G.-N.; Xu, L.-P. Degradation pattern and element distribution of WE43 magnesium alloy implanted in rats. *Jieyou Xuebao* **2010**, *41*, 425–429. [[CrossRef](#)]
52. Krause, A.; von der Hoh, N.; Bormann, D.; Krause, C.; Bach, F.W.; Windhagen, H.; Meyer-Lindenberg, A. Degradation behaviour and mechanical properties of magnesium implants in rabbit tibiae. *J. Mater. Sci.* **2010**, *45*, 624–632. [[CrossRef](#)]
53. Gunde, P.; Furrer, A.; Hanzl, A.C.; Schmutz, P.; Uggowitzer, P.J. The influence of heat treatment and plastic deformation on the bio-degradation of a Mg–Y–RE alloy. *J. Biomed. Mater. Res. A* **2010**, *92*, 409–418. [[CrossRef](#)]
54. Windhagen, H.; Radtke, K.; Weizbauer, A.; Diekmann, J.; Noll, Y.; Kreimeyer, U.; Schavan, R.; Stukenborg-Colsman, C.; Waizy, H. Biodegradable magnesium-based screw clinically equivalent to titanium screw in hallux valgus surgery: Short term results of the first prospective, randomized, controlled clinical pilot study. *Biomed. Eng. Online* **2013**, *12*, 62. [[CrossRef](#)]
55. Zumdick, N.A.; Jauer, L.; Kersting, L.C.; Kutz, T.N.; Schleifenbaum, J.H.; Zander, D. Additive manufactured WE43 magnesium: A comparative study of the microstructure and mechanical properties with those of powder extruded and as-cast WE43. *Mater. Charact.* **2019**, *147*, 384–397. [[CrossRef](#)]
56. Zhou, L.; Liu, Y.; Zhang, J.; Kang, Z. Microstructure and mechanical properties of equal channel angular pressed Mg–Y–RE–Zr alloy. *Mater. Sci. Technol.* **2016**, *32*, 969–975. [[CrossRef](#)]
57. Liu, H.-H.; Ning, Z.-L.; Sun, H.-C.; Cao, F.-Y.; Wang, H.; Zhao, X.-Y.; Sun, J.-F. Microstructure and elevated-temperature tensile properties of differential pressure sand cast Mg-4Y-3Nd-0.5Zr alloy. *China Foundry* **2016**, *13*, 30–35. [[CrossRef](#)]
58. Stanford, N.; Barnett, M. Effect of composition on the texture and deformation behaviour of wrought Mg alloys. *Scr. Mater.* **2008**, *58*, 179–182. [[CrossRef](#)]
59. Laser, T.; Hartig, C.; Nürnberg, M.R.; Letzig, D.; Bormann, R. The influence of calcium and cerium mischmetal on the microstructural evolution of Mg–3Al–1Zn during extrusion and resulting mechanical properties. *Acta Mater.* **2008**, *56*, 2791–2798. [[CrossRef](#)]
60. Kleiner, S.; Uggowitzer, P.J. Mechanical anisotropy of extruded Mg–6% Al–1% Zn alloy. *Mater. Sci. Eng. A* **2004**, *379*, 258–263. [[CrossRef](#)]
61. Mackenzie, L.W.F.; Davis, B.; Humphreys, F.J.; Lorimer, G.W. The deformation, recrystallisation and texture of three magnesium alloy extrusions. *Mater. Sci. Technol.* **2007**, *23*, 1173–1180. [[CrossRef](#)]
62. Stanford, N.; Barnett, M.R. The origin of “rare earth” texture development in extruded Mg-based alloys and its effect on tensile ductility. *Mater. Sci. Eng. A* **2008**, *496*, 399–408. [[CrossRef](#)]
63. Jin, W.H.; Wu, G.S.; Li, P.H.; Chu, P.K. Improved corrosion resistance of Mg–Y–RE alloy coated with niobium nitride. *Thin Solid Film.* **2014**, *572*, 85–90. [[CrossRef](#)]
64. Ott, N.; Schmutz, P.; Ludwig, C.; Ulrich, A. Local, element-specific and time-resolved dissolution processes on a Mg–Y–RE alloy—Influence of inorganic species and buffering systems. *Corros. Sci.* **2013**, *75*, 201–211. [[CrossRef](#)]
65. Jones, D.A. *Principles and Prevention of Corrosion*; Prentice Hall: Upper Saddle, NJ, USA, 1996.

